

SCIENTIFIC REPORTS



OPEN

Structural basis of substrate recognition by a novel thermostable (*S*)-enantioselective ω -transaminase from *Thermomicrobium roseum*

Sunghark Kwon¹, Jun Hyuck Lee², Chang Min Kim¹, Hyunseok Jang¹, Hyungdon Yun³, Ju-Hong Jeon⁴, Insuk So⁴ & Hyun Ho Park¹

Transaminases catalyze the reversible transfer reaction of an amino group between a primary amine and an α -keto acid, utilizing pyridoxal 5'-phosphate as a cofactor. ω -transaminases (ω TAs) recognize an amino group linked to a non- α carbon of amine substrates. Recently, a novel (*S*)-enantioselective ω TA from *Thermomicrobium roseum* (Tr- ω TA) was identified and its enzymatic activity reported. However, the detailed mechanism of (*S*)-enantioselective substrate recognition remained unclear. In this study, we determined the crystal structure of Tr- ω TA at 1.8 Å resolution to elucidate the mechanism underlying Tr- ω TA substrate (*S*)-enantioselectivity. A structural analysis of Tr- ω TA along with molecular docking simulations revealed that two pockets at the active site tightly restrict the size and orientation of functional groups of substrate candidates. Based on the structural information and docking simulation results, we propose a comprehensive catalytic mechanism of Tr- ω TA. The present study thus provides structural and functional insights into the (*S*)-enantioselectivity of Tr- ω TA.

Transaminases reversibly catalyze the transfer reaction of an amino group from an amine donor to a carbonyl acceptor, mediated by pyridoxal 5'-phosphate (PLP) as a cofactor. These enzymes are classified by diverse criteria including fold type (I and IV), sequence pattern (I–IV), and amino group position of the donor substrate (α , β , γ , and ω)^{1,2}. α -, β -, and γ -transaminases recognize substrates containing an amino group bound to α , β , and γ carbon atoms, respectively². ω -transaminases (ω TAs), in contrast, constitute the comprehensive enzymes that transfer an amino group bound to a non- α carbon of amine substrates^{1,2}. ω TAs have gained considerable attention owing to their enantioselectivity, which is considered as a key property in the field of pharmaceutical chemistry and the fine chemical industry^{3–5}. Industrial applications of ω TAs have been attained through both kinetic resolution and asymmetric synthesis. For kinetic resolution, undesired enantiomers comprising half of the produced racemic compounds are converted to ketone products, leaving the remaining, preferred enantiomers in their native form³. For asymmetric synthesis, preferred ketone compounds accept an amino group, yielding the desired chiral amines³.

This unique enzymatic property of ω TAs has led to active structural studies regarding the enantioselectivity of ω TAs. The active site geometry formed with PLP has been considered as a determinant factor for the enantioselectivity^{6–8}. The amino group transfer accompanying PLP comprises two consecutive half reactions^{6,7}, with the first being the oxidative deamination process of a primary amine. The second half reaction, in contrast, proceeds via the reductive amination process of a ketone compound. PLP is involved in both reactions as a mediator of the amino group. The amination reaction is initiated by substituting the amino group from an amine donor for the ϵ -amino group of a Lys residue covalently bound to the C4' atom on PLP, resulting in the formation of

¹College of Pharmacy, Chung-Ang University, Dongjak-gu, Seoul, 06974, Republic of Korea. ²Unit of Polar Genomics, Korea Polar Research Institute, Incheon, 21990, Republic of Korea. ³Department of Systems Biotechnology, Konkuk University, Seoul, 05029, Republic of Korea. ⁴Department of Physiology and Biomedical Sciences, Institute of Human-Environment Interface Biology, Seoul National University College of Medicine, Jongno-gu, Seoul, 03080, Republic of Korea. Correspondence and requests for materials should be addressed to H.H.P. (email: xrayleox@cau.ac.kr)

pyridoxamine-5'-phosphate (PMP). The amino group of PMP is transferred to a ketone compound as an amino group acceptor via the second half reaction. In both reactions, PLP/PMP is located in the PLP/PMP binding site through coordination with adjacent residues. The spatial position of PLP primarily determines the enantioselectivity peculiar to each ω TA by favorably orienting toward the substrate entry direction between the *Re*- and *Si*-faces⁹. Previous structural studies have revealed that ω TAs have two pockets (the P- and O-pockets) in the active site^{2,5,10}. The P-pocket is located near the phosphate group of PLP, whereas the O-pocket is positioned in the proximity of the O3' atom on PLP. The two pockets differ from each other in size, depending on the class of ω TAs^{5,8}. The resulting volumetric difference renders the substrate recognition more stringent regarding enantioselectivity^{5,8,10}.

ω TAs belonging to fold type I and class III exhibit (S)-enantioselectivity². Several (S)-enantioselective ω TAs have been identified on the basis of sequence and biochemical analyses^{11–19} along with structural studies^{10,20–23}. An (S)-enantioselective ω TA from *Vibrio fluvialis* (Vf- ω TA) has also been engineered by incorporating unnatural amino acids, thereby improving its thermostability and resistance to organic solvents²⁴. Recently, the structures of Vf- ω TA were determined with its apo²⁵ and holo²⁶ forms. Based on the sequence information of Vf- ω TA, a novel thermostable (S)-specific transaminase from *Thermomicrobium roseum* (Tr- ω TA) was also identified that exhibits diverse substrate specificity and thermostability²⁷. This previous study revealed that Tr- ω TA demonstrates (S)-enantioselectivity and different enzymatic activities according to the size and physicochemical properties of its functional groups²⁷.

However, the molecular mechanism through which Tr- ω TA possesses (S)-enantioselective substrate specificity is not fully understood. It also remains elusive how Tr- ω TA can recognize diverse substrates as an amino group donor. Moreover, although many ω TAs exploit pyruvate as an amino group acceptor, little is known regarding the spatial position and interaction at the active site during catalysis. These issues require detailed explanations at the molecular level. Thus, it is necessary to elucidate the structure of Tr- ω TA and the mechanism of binding to its substrates.

Herein, we report the crystal structure of Tr- ω TA at 1.8 Å resolution to clarify the substrate recognition mechanism of (S)-enantioselective Tr- ω TA. Along with structural analyses, molecular docking simulations were performed with various substrate candidates. The structural analysis revealed that two pockets at the active site of Tr- ω TA are formed with evolutionarily conserved residues. The docking simulations suggested that key residues at the active site are spatially arranged to recognize the functional groups of each substrate compound. Our results, thus, provide structural insight into the substrate recognition mechanism of (S)-enantioselective Tr- ω TA.

Results and Discussion

Overall structure of Tr- ω TA. The structure of Tr- ω TA was determined in the PMP-bound form at 1.8 Å resolution. Data collection and refinement statistics for Tr- ω TA are presented in Table 1. The overall structure constitutes a homodimer, with each subunit comprising a large and a small domain (Fig. 1). The large domain (residues 94–315) contains a PMP cofactor and consists of eleven helices and seven strands, adopting an α - β - α sandwich fold (Fig. 1b,c). The central β -strands form a twisted β -sheet, in which six strands, except the β 11 strand, run parallel to each other (Fig. 1b,c). Two of the eleven helices comprise 3₁₀-helices, of which the η 3 helix contains the Lys289 residue involved in the catalytic reaction. The small domain can be divided into two lobes (N- and C-terminal lobes), which contain the corresponding terminal regions (Fig. 1b,c). The N-terminal lobe is comprised of an antiparallel β -sheet and four helices. Notably, the β -sheet is flanked by the C-terminal lobe and the α 4 helix runs perpendicular across the β -sheet. The region between α 4 and α 5 interacts with the other subunit, playing a crucial role in forming the active site of the one subunit. The C-terminal lobe also contains an antiparallel β -sheet formed by four strands. A notable feature of the C-terminal lobe is that the α 14 helix and a relatively long linker connected to the large domain are located away from the rest of the cluster of the C-terminal lobe (Fig. 1b), with the linker being responsible for forming the PLP-binding site in the other subunit.

The crystal structure of Tr- ω TA revealed that Tr- ω TA exists as a homodimer in the asymmetric unit. A plethora of residues are involved in interactions between each subunit (Fig. 2a,b). Several structured loops from the two subunits interact with each other at the interface, forming a tight loop insertion between the two subunits (Fig. 2c). These interactions indicated that Tr- ω TA is stable as a dimer form owing to the strong binding. A size exclusion chromatography-coupled multiangle light scattering (SEC-MALS) analysis also showed that a peak appeared at 15 ml retention volume, which indicated that Tr- ω TA exists as a dimer in solution (Fig. 2d). Moreover, a multimeric prediction using the PDBePISA server²⁸ suggested that the most probable multimeric state of Tr- ω TA is a dimer in solution. These results coincided with the dimer form revealed by the crystal structure, strongly implying that Tr- ω TA carries out its biological function as a dimer.

Incorporating a cofactor into the active site has been shown to have an effect on conformational changes in partial regions of Vf- ω TA²⁵. In our structure, PMP was observed only in subunit B. This finding raised the possibility that conformational differences might exist between the two subunits of Tr- ω TA. Accordingly, to investigate potential structural differences between the two subunits that form the dimer, their overall structures were compared (Supplementary Fig. S1). A structural superimposition analysis showed that the root-mean-square deviation (RMSD) value for 440 C α atoms of each subunit was 0.71 Å. This RMSD value signified that the two subunits of Tr- ω TA are structurally almost identical to each other. As a result, although the PMP molecules were discriminatorily distributed between the subunits in the crystal, this did not cause any structural differences in the dimer form. It was thus inferred that the strong interactions between the two subunits could offset the structural dynamics induced by the absence of PMP.

The surface electrostatic potential of Tr- ω TA was also assessed to investigate the spatial distribution of charged residues. Notably, we found that positively charged residues are dominantly distributed on the flat area including the entrance to the active site, whereas negatively charged residues are spread out on the peripheral “wall” structure surrounding the flat area (Fig. 3). However, the opposite side of the flat area did not exhibit any special

Data collection	
Space group	R3
Unit cell parameter <i>a</i> , <i>b</i> , <i>c</i> (Å)	
<i>a</i> , <i>b</i> , <i>c</i> (Å)	<i>a</i> = <i>b</i> = 118.3, <i>c</i> = 170.5
α , β , γ (°)	α = β = 90, γ = 120
Resolution range (Å) ^a	50.00–1.80 (1.83–1.80)
Total reflections	568364
Unique reflections	81838
Multiplicity	6.9 (6.9)
Completeness (%) ^a	99.8 (99.2)
Mean <i>I</i> / σ (<i>I</i>) ^a	30.6 (2.9)
<i>R</i> _{merge} (%) ^{a,b}	9.6 (89.3)
Wilson <i>B</i> -factor (Å ²)	20.3
Refinement	
Resolution range (Å)	43.90–1.80
Reflections	81813
Reflections (test set)	4099
<i>R</i> _{work} (%)	15.3
<i>R</i> _{free} (%)	15.5
No. of molecules in the asymmetric unit	2
No. of protein atoms/water molecules	6925/782
Average <i>B</i> -factor values of protein/water (Å ²)	21.8/34.4
Ramachandran plot:	
favored/outliers (%)	97.6/0.0
Rotamer outliers (%)	0.0
RMSD bonds (Å)/angles (°)	0.004/0.75

Table 1. Data collection and refinement statistics for Tr- ω TA. ^aValues for the outermost resolution shell in parentheses. ^b $R_{\text{merge}} = \sum_h \sum_i |I(h)_i - \langle I(h) \rangle| / \sum_h \sum_i I(h)_i$, where *I*(*h*) is the observed intensity of reflection *h*, and $\langle I(h) \rangle$ is the average intensity obtained from multiple measurements.

features. This finding implied that the electric field generated in the vicinity of the active site may play an essential role in inducing the substrates into the active site (as discussed in further detail later in this report).

Active site of Tr- ω TA. The active site of ω TAs is located at the interface between two subunits; moreover, some residues from one subunit are directly associated with the formation of the active site of the other subunit^{1,2}. The entrance to the active site is also positioned near the interface. Another notable structural feature of ω TAs is the relatively deep funnel located between the entrance and the PLP-binding site^{1,2}. These distinctive active site structural traits are conserved in Tr- ω TA (Fig. 4a,b).

The chemical modification state of PLP is important throughout the catalytic reaction of ω TAs because PLP plays an essential role as an amino group mediator^{2,6}. The amino group transfer mechanism of ω TAs had been partially proposed on the basis of previously accumulated findings². In the “rest period” of the catalysis, the C4' atom of PLP covalently binds to the ϵ -amino group of an adjacent Lys residue, forming a Schiff base (the internal aldimine state). Subsequently, an amino group from a primary amine is substituted for the ϵ -amino group of the Lys residue, followed by the formation of PMP (the Michaelis complex state). In the Michaelis complex, consequently, PMP binds to neither the substrate nor the Lys residue. In this regard, determining whether a cofactor molecule in a crystal structure is PLP or PMP is significant because it provides decisive information to infer which step the structure corresponds to in the catalytic cycle.

In the crystal structure of Tr- ω TA, the cofactor molecule did not link to either the Lys289 residue or a possible substrate, suggesting that the cofactor was PMP (Fig. 4c). To further verify this conclusion, a UV-Visible spectrometric analysis of Tr- ω TA was also carried out to obtain the absorption spectrum of the cofactor. A previous study demonstrated that the PMP-bound form in a TA from *Thermoproteus uzoniensis* has an absorption peak at approximately 330 nm, whereas the absorption peak in the PLP-bound form appears in the proximity of 420 nm²⁹. As shown in Fig. 4d, Tr- ω TA exhibited an absorption pattern at approximately 330 nm. This spectrometric result was in agreement with the PMP-absorption wavelength reported in the previous study²⁹, confirming that the crystal structure of Tr- ω TA constituted the PMP-bound form.

The electron density of PMP is relatively poor as compared with that of K289 (Fig. 4c). Moreover, a series of omit maps of PMP at sequential sigma levels showed that the density signal of PMP is weak (Supplementary Fig. S2a–c), indicating that PMP exists at a lower molar ratio than the peptide component in the crystal. Additionally, to estimate the occupancy value of PMP, PMP-calculated $2F_o - F_c$ and $F_o - F_c$ maps were generated with various occupancy values (0.83–0.25). We found that the PMP-calculated $F_o - F_c$ map shows the least electron density as both positive and negative maps at the 3 sigma level along with the clear $2F_o - F_c$ map, when the occupancy value is set to 0.75 (Supplementary Fig. S2d,e). Consequently, the occupancy value of PMP in our

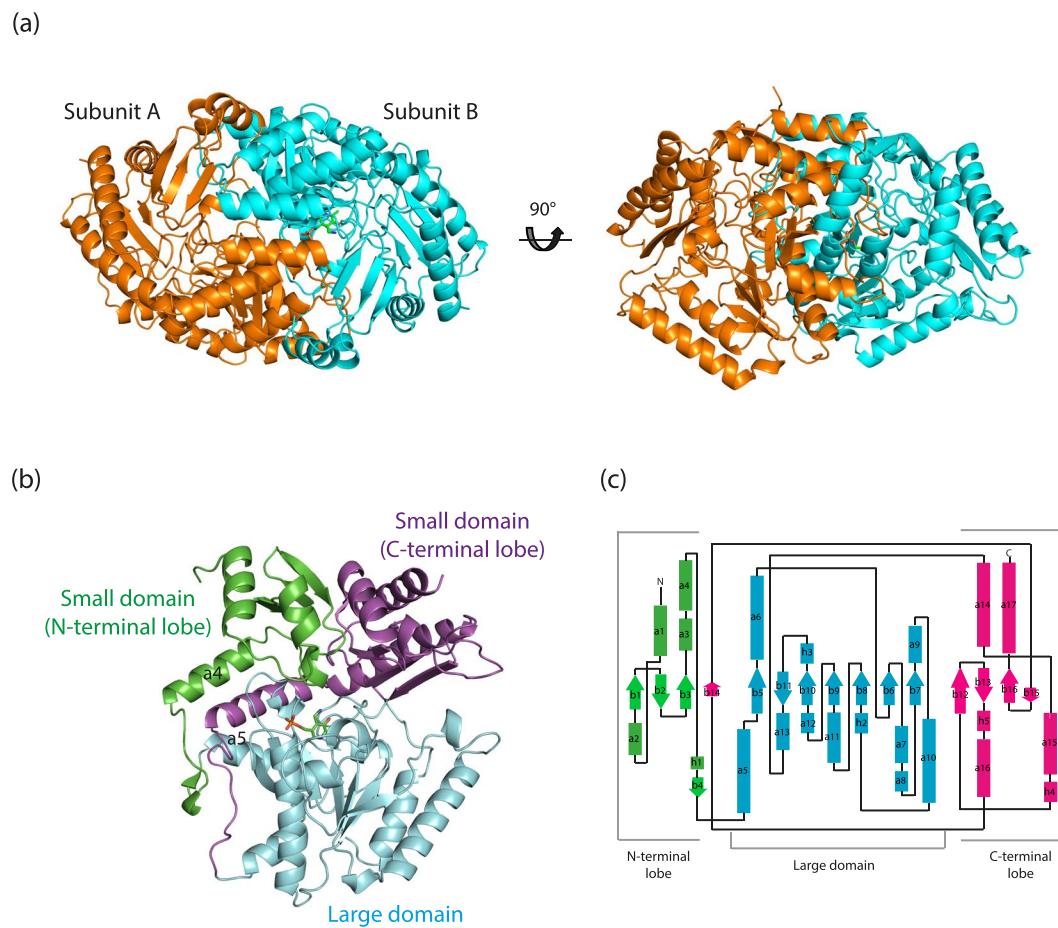


Figure 1. Overall structure of Tr- ω TA. **(a)** Overall structure of Tr- ω TA. The structure as a dimer form is depicted as a cartoon and viewed from two different directions. Subunits A and B are coloured orange and cyan, respectively. The PMP molecule in subunit B is represented as green sticks. **(b)** The two domains of Tr- ω TA (subunit B): large domain (residues 94–315; cyan), small domain (residues 1–93 and 316–451). The small domain is divided into two lobes (N- and C-terminal lobes): N-terminal lobe (residues 1–93; green) and C-terminal lobe (residues 316–451; magenta). **(c)** Topology diagram of Tr- ω TA. Helices and β -strands are depicted as rectangles and arrows, respectively.

structure is assumed to be approximately 0.75. As PMP is present only in subunit B in the crystal structure, our crystal therefore likely constituted a mixture of the apo and holo forms of Tr- ω TA. The scarcity of PMP in the crystal may result from loss during the purification and crystallization consequent to diffusion of PMP into the buffer solutions.

The Tr- ω TA structure also revealed that PMP is chemically linked to neighboring water molecules and residues (Supplementary Fig. S3). Specifically, the oxygen atoms in the phosphate group of PMP are coordinated to adjacent water molecules and residues such as Gly121, Ala122, and Thr323. The nitrogen atom on the PMP ring forms a hydrogen bond with Asp260. The hydroxyl group of the PMP also forms a hydrogen bond with a water molecule coordinated to Glu227 and Ala232, and the nitrogen atom linked to the C4' atom binds to a water molecule as well. Overall, the PMP molecule is coordinated to the proximal residues via hydrogen bonds, part of which are mediated by water molecules. Accordingly, the hydrogen-bond network serves as a main factor underlying PMP coordination in the active site. It was also found that the carbon atoms on PMP form hydrophobic interactions with nearby hydrophobic residues such as Gly156, Val262, Ile263, and Phe322. Notably, Thr323 and Tyr324 from the other subunit contribute to the stabilization of the PMP position. This finding suggested that the dimer formation of Tr- ω TA is therefore indispensable to the catalytic activity.

The differently sized P- and O-pockets that comprise the ω TA active site^{2,5,10} are located in the proximity of the phosphate and the phenol group of PLP/PMP, respectively, and their relative sizes are dependent on the fold type and class of ω TAs^{5,8}. In the case of Tr- ω TA, we found that the P-pocket is larger than the O-pocket (Fig. 4e). This implied that a bulkier functional group of (S)-enantioselective substrates would be oriented toward the P-pocket, whereas a smaller functional group is assigned to the O-pocket.

Structural comparison with Vf- ω TA. The structure of Tr- ω TA was compared with that of Vf- ω TA (PDB ID: 4E3Q), which has a high sequence similarity (sequence identity = 41%)²⁷. The structural comparison revealed that the two TAs are structurally almost identical to each other, sharing an overall architecture (Fig. 5a). The

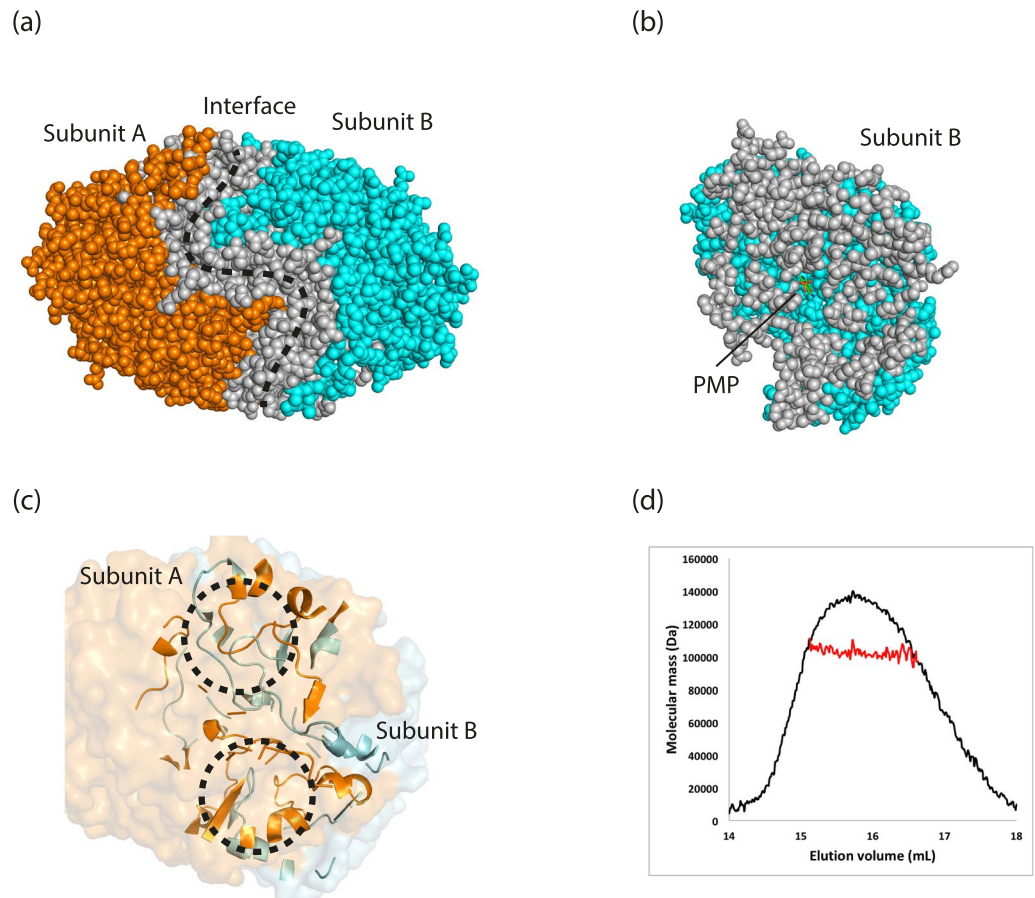


Figure 2. Dimer formation of Tr- ω TA. (a) Interactions between the two subunits of Tr- ω TA. Subunit A, B, and the interface are represented as orange, cyan, and grey spheres, respectively. (b) A cross section of subunit B containing PMP. PMP is depicted as sticks. (c) Loop insertion at the interface. The black dashed circles indicate inserted loops between the two subunits. The colour code is the same as in panel a. (d) SEC-MALS profile of Tr- ω TA. SEC-coupled MALS data (red) are plotted as elution volume and molecular mass distributions, and superimposed on the SEC chromatogram (black) at 280 nm.

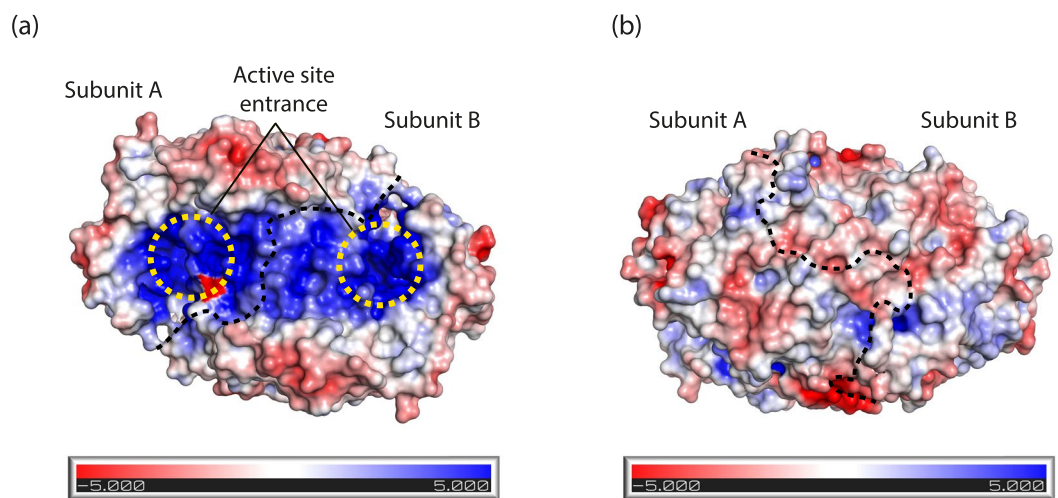


Figure 3. Surface electrostatic potential of Tr- ω TA. Surface electrostatic distribution is represented in two different orientations. The scale ranges from -5 kT/e (red) to 5 kT/e (blue). Electrostatic potential on the surface representing the active site entrances (a) and on the reverse side of panel a (b). The yellow dotted circles in panel a denote the active site entrances. The dashed curves indicate a boundary between the two subunits.

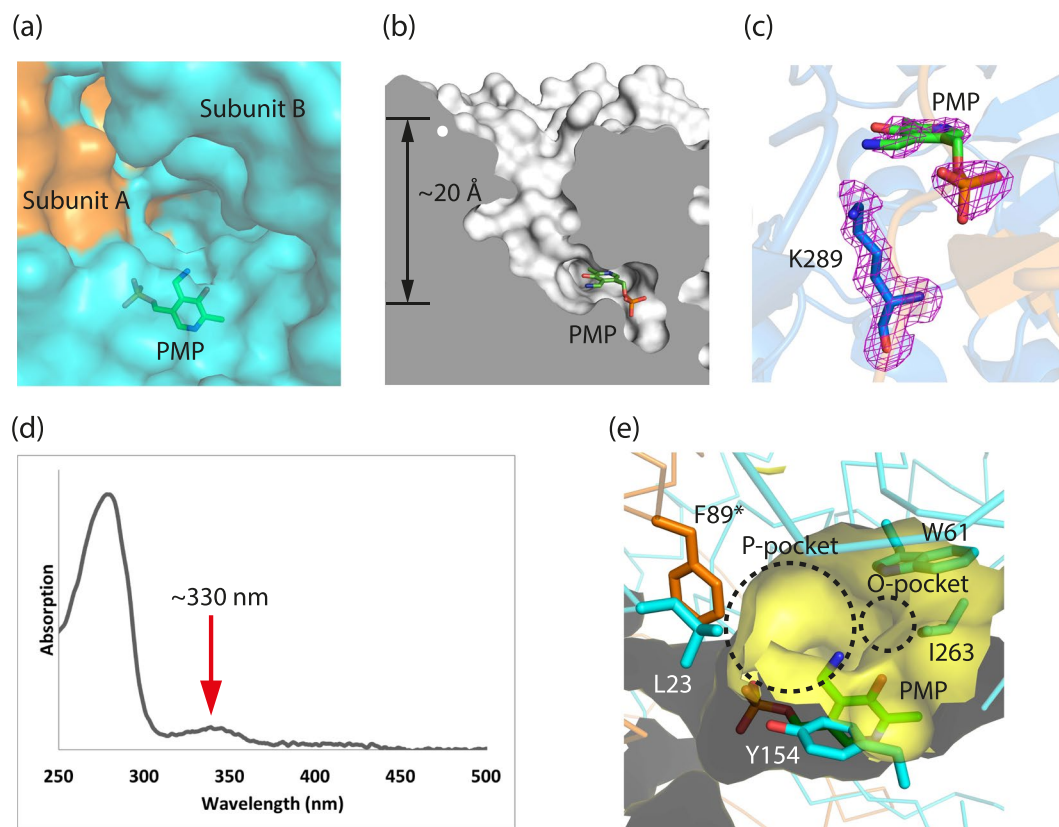


Figure 4. PMP-incorporated active site of Tr- ω TA. **(a)** Active site cavity of Tr- ω TA. The PMP cofactor is positioned in the vicinity of the interface of the two subunits. Some residues from subunit A are involved in the formation of the active site of subunit B. The apo enzyme and PMP are represented as surface and stick (green) modes, respectively. Subunit A and B are colored orange and cyan, respectively. **(b)** A cross section representing a funnel to the active site. The PMP cofactor is located in the bottom of the long funnel. Tr- ω TA is depicted as a surface (white) mode. **(c)** Omit map of PMP and Lys289. The omit map ($F_o - F_c$) is colored magenta and contoured at the 2.0 sigma level. **(d)** UV-Visible spectrum of Tr- ω TA. The red arrow indicates the peak position at approximately 330 nm. **(e)** The P- and O-pockets in the active site. The apo enzyme except for the active site (yellow surface and sticks) is represented in ribbon. Subunits A and B are colored orange and cyan, respectively. The asterisk of the F89 residue denotes a residue from the other subunit.

RMSD value for the two TAs (each of 440 C α atoms) was 1.5 Å. The geometries of the active sites containing PMP were also in accordance (Fig. 5b), which suggested that Tr- ω TA may exhibit the same catalytic properties as Vf- ω TA.

Despite the structural and functional similarities, however, it was reported that Tr- ω TA exhibits an outstanding thermostability as compared with that of Vf- ω TA²⁷. As protein mobility has been highlighted as an important factor contributing to temperature tolerance³⁰, we analysed the B-factor distribution of the two TAs. This analysis showed that the structure of Vf- ω TA exhibits overall low B-factor values (Fig. 5c). In contrast, the loop covering the active site of Tr- ω TA exhibited high B-factor values (Fig. 5d), suggesting that this loop likely manifests intrinsic flexibility. This finding implied that the high mobility loop may play a key role in maintaining the structure of the active site by alleviating thermal perturbation caused by high temperature.

Molecular docking simulations. Although the enantioselectivity of Tr- ω TA, a fold type I- and class III- ω TA, has been demonstrated²⁷, the molecular mechanism has remained unclear. To obtain structural insight into (S)-enantioselective substrate recognition, we performed molecular docking simulations. Energetically favorable conformers of several compounds including S and R forms were investigated. Specifically, we selected (S)-enantioselective compounds reported as exhibiting relatively low and high activities in the previous study²⁷; the (R)-enantiomers of the compounds with high activities were also prepared.

To more accurately run the docking simulations, some residues related to the active site were designated as flexible residues. The active site residues of (S)- enantioselective ω TAs have been identified on the basis of sequence alignment and docking simulation studies⁷. The putative active site residues of Tr- ω TA were also revealed by multiple sequence alignment with other ω TAs (Supplementary Fig. S4). For Tr- ω TA, Y154 along with L23 and F89 from the other subunit constitute the P-pocket components, whereas W61 and I263 are involved in the formation of the O-pocket. Additionally, K289 is assumed to play a crucial role in forming a Schiff base with PLP. An arginine residue corresponding to R416 has also been shown to be responsible for substrate binding³¹. Thus, these seven residues were set as flexible residues for the docking simulations. PMP in the structure was

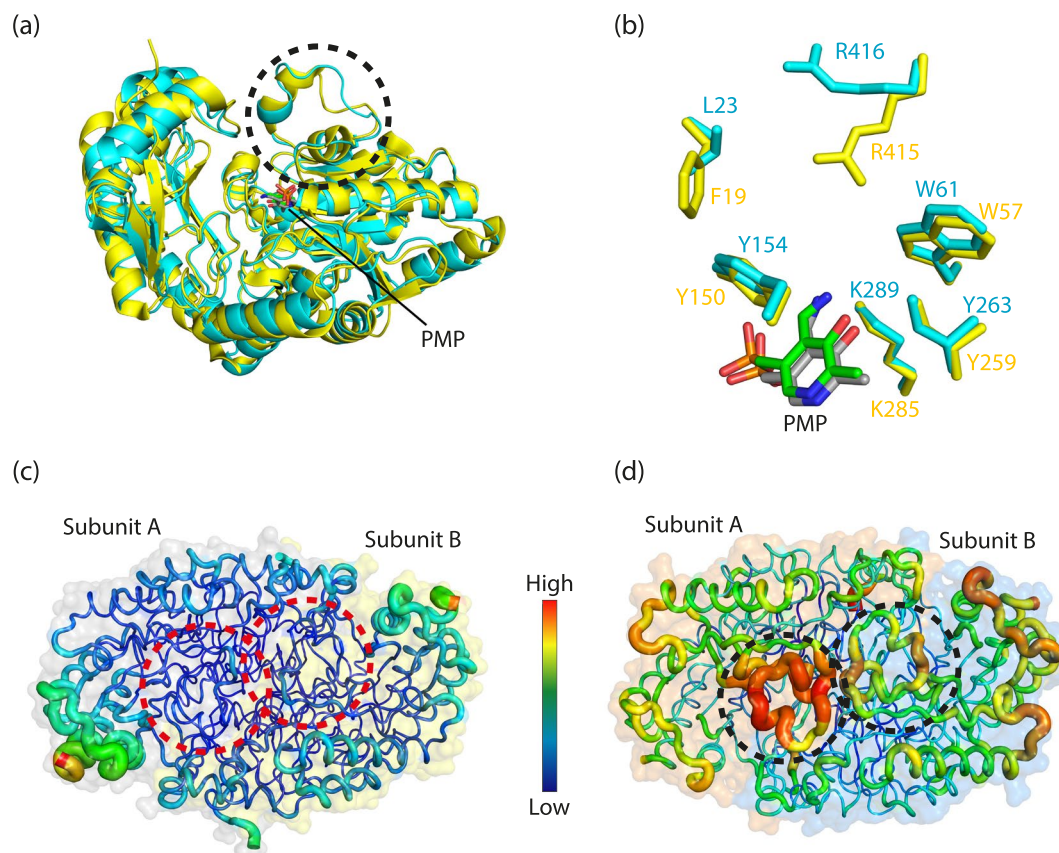


Figure 5. Structural comparison of Tr- ω TA with Vf- ω TA. **(a)** Overall structural comparison between Tr- ω TA and Vf- ω TA. Subunit B of Vf- ω TA is superimposed onto that of Tr- ω TA. The structures of Tr- ω TA and Vf- ω TA are colored cyan and yellow, respectively. The apo enzymes and PMP are shown in cartoon and stick representations, respectively. **(b)** Zoom-in view of the PMP cofactor in a different orientation. The PMP molecules and key residues of the active site are shown. The PMP cofactors of Tr- ω TA and Vf- ω TA are colored green and grey, respectively. **(c)** B -factor distribution of Vf- ω TA **(c)** and Tr- ω TA. **(d)** The two structures are depicted in putty representation and rainbow-colored from red to violet in B -factor value order. The dashed circles correspond to those in panel a.

replaced with PLP in a Schiff base state for accurate docking simulations. The selected compounds were docked into the active site of Tr- ω TA under the same conditions.

Each compound and its binding energy are listed in Supplementary Table S1. Notably, as the binding energy values of the compounds with the same formula are similar regardless of enantioselectivity, the docking products can be assessed only on the basis of their conformations. The four compounds with positive relative activities exhibited similar functional group orientations (Fig. 6a–d). Their bulky groups and short groups were oriented toward the P-pocket and O-pocket, respectively. In particular, the two fluorine atoms of compound 2 were shown to form hydrogen bonds with W61 and Y154 (Fig. 6b). A previous study demonstrated that a 1,3-proton transfer reaction mediated by the ϵ -amino group of the Lys key residue in the active site is a rate-determining step³². This reaction corresponds to the α -proton removal from an amino group donor (external aldimine) by the Lys residue and the subsequent α -proton transfer to the C4' carbon atom of the cofactor (ketimine), which leads to the formation of the Michaelis complex via addition of a water molecule. Accordingly, considering that the spatial accession of the α -proton to the ϵ -amino group of the Lys residue is important for the general base catalysis, the binding modes of the substrate compounds notably for orientation and distance toward the Lys residue are assumed to be crucial for catalysis. In conclusion, these binding modes appeared to be appropriate as binding poses for substrate binding and catalysis. Moreover, these results coincided with the previous activity profiles for each compound²⁷.

To investigate the substrate suitability of the (*R*)-enantiomer, the (*R*)-enantiomer for (*S*)-compound 2 was also prepared and subjected to a docking simulation. As shown in Fig. 6e, the orientations of its two functional groups were opposite to those of the (*S*)-enantiomer. In this binding pose, the amino group was placed away from the position of PLP. It also appeared that it was difficult for the small functional group to bind to the O-pocket. In addition, (*S*)-compounds with low relative activities showed inappropriate poses for the pockets and PLP (Fig. 6f–h). Thus, it was concluded that the binding of two functional groups to the two pockets and the orientation of an amino group depended on the size of the functional groups and the enantioselectivity of the compounds.

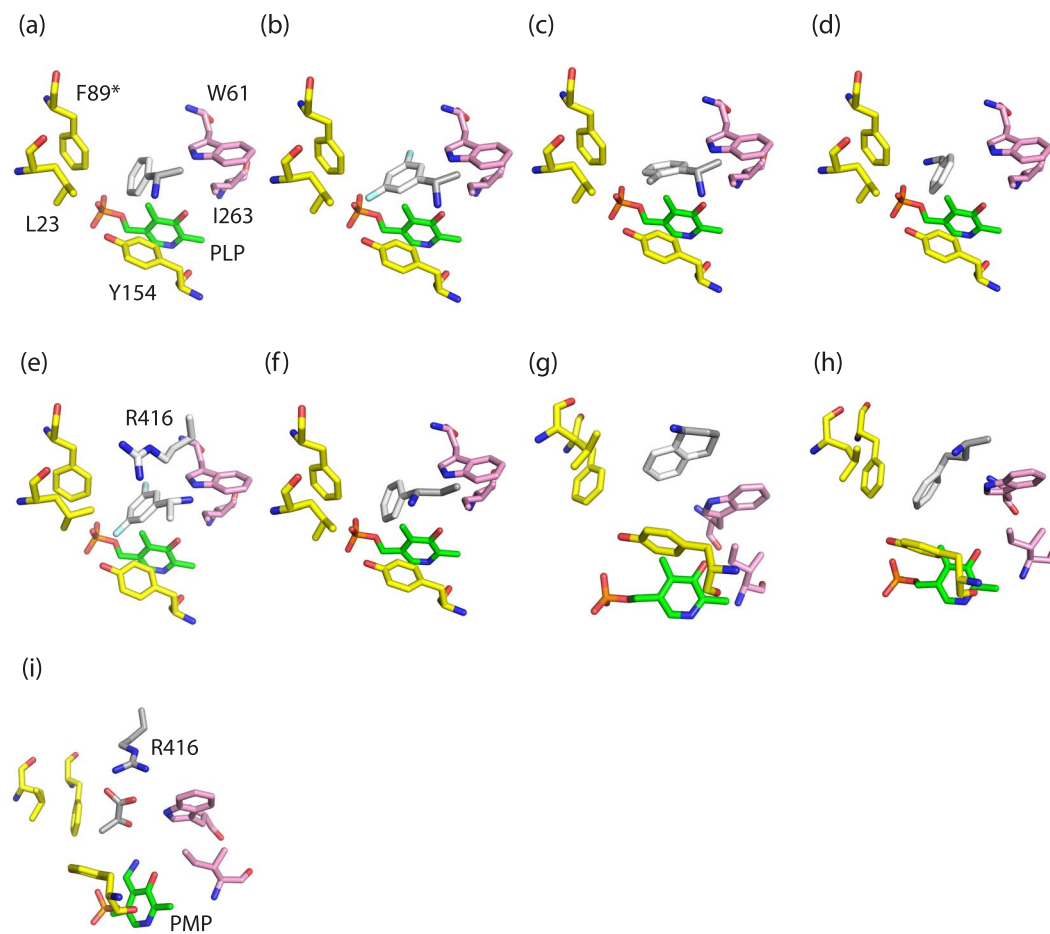


Figure 6. Predicted binding poses of the top scoring conformers. All the conformers, the active site residues, and the cofactor are shown in stick representation. The P-pocket is composed of L23, F89, and Y154, and colored yellow. The asterisk of F89 denotes a residue from the other subunit. The O-pocket consists of W61 and I263, and is colored pink. The cofactor and conformers are colored green and grey, respectively. The residue configurations in the active site are represented with the top scoring conformers for (S)-compound 1 (a) 2 (b) 3 (c) 4 (d) (R)-compound 2 (e) (S)-compound 5 (f) 6 (g) 7 (h) and pyruvate (i).

For class-III ω TAs, pyruvate can function as an amino group acceptor^{1,2}. However, the structural mechanism at the molecular level is not fully understood. In the present study, we performed docking simulations of pyruvate to obtain structural insight into the transfer of an amino group to pyruvate. PMP was utilized in the structure as for the docking simulations. Notably, we found that the carboxylic acid of pyruvate interacts with the guanidino group of R416, resulting in the proper orientation of the ketone group toward PMP with a stable pose in the hydrophobic active site (Fig. 6i). From the viewpoint of thermodynamics, the entry of pyruvate into the active site of Tr- ω TA would cause an entropic decrease. Consequently, this would appear to result in an increase of free energy upon pyruvate binding. However, such a seemingly unfavorable phenomenon might be explained by the compensation of enthalpy. It is reasonable to assume that a hydrophilic substrate such as pyruvate would be able to maintain a thermodynamically stable state by increasing the number of binding points to adjacent residues, thereby decreasing enthalpy under thermodynamically unfavorable circumstances such as within the hydrophobic active site.

Amino group transfer mechanism of Tr- ω TA. Two substrates are necessary for the completion of the transamination reaction by TAs using PLP as a cofactor. Notably, both PLP and pyruvate have strong negative charges, which supports the likelihood of a mechanism by which the charged molecules are induced into the active site of Tr- ω TA. Our surface electrostatic potential analysis revealed that positively charged residues are distributed in the proximity of the active site (Fig. 3), thereby generating a potent electric field (Fig. 7). This electric field may play a pivotal role in attracting PLP and pyruvate into the active site. In addition, we also found that hydrophobic residues are dominantly distributed in the interior as well as at the entrance of the active site (Supplementary Fig. S5). The distribution of these hydrophobic residues in the active site may constitute a useful strategy for favorably disposing PLP and the substrates in the active site by obstructing inappropriate interactions with the charged molecules.

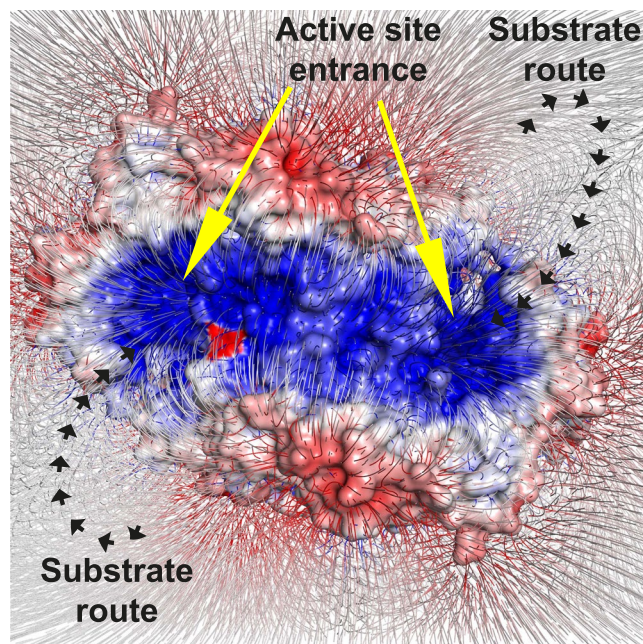


Figure 7. Electric field generation of Tr- ω TA. Surface electrostatic potential is represented in the same method as in Fig. 3. The electric field map grad is contoured at the -0.5 sigma level.

This assumption is supported by a previously published example regarding acetylcholinesterase, wherein this enzyme was reported to exhibit a strong electrostatic dipole³³. This study raised the possibility that the electric field induces the charged substrate into the active site of acetylcholinesterase and that aromatic residues in the active site are associated with the formation of a proper binding site. Another study demonstrated that electrostatic properties near the binding sites of enzymes such as superoxide dismutase, acetylcholinesterase, and barnase are associated with electrostatic steering for the substrate binding³⁴. This study showed that introduction of charged residues near the active site increased enzyme-substrate association rates, implying electrostatic enhancement. The results were reproduced using Brownian dynamics simulations based on the finite-difference linearized Poisson-Boltzmann equation. In turn, Tr- ω TA may constitute another example demonstrating the importance of an electric field with respect to transporting a substrate into its active site.

TAs including Tr- ω TA exhibit the enzymatic property to sequentially recognize two different substrates at the same active site. Accordingly, the transamination reaction of Tr- ω TA comprises two consecutive processes: amino group donation and acceptance (Fig. 8). Herein, we propose a comprehensive transamination mechanism including these two processes. As the initial step, a nucleophilic attack from the first substrate as an amino group donor allows the Lys289 residue to depart from the bound PLP molecule, forming a new Schiff base between the substrate and PLP. A straightforward base abstraction of the α -proton by the Lys289 residue causes electronic rearrangement in the external aldimine step. After the acceptance of a proton from the Lys289 residue, a hydrolysis reaction occurs, producing the Michaelis complex and a ketone compound. Then, the second process is initiated through the use of pyruvate as an amino group acceptor. Interacting with the R416 residue, pyruvate forms a ketimine with PMP. The second proton acceptance from the Lys289 residue occurs along with electron rearrangement, resulting in the second external aldimine. Finally, imination is attained between the Lys289 residue and PLP, recovering the initial internal aldimine.

In summary, we determined the crystal structure of Tr- ω TA specific to (*S*)-enantiomers. Surface electrostatic potential analysis revealed that Tr- ω TA likely exploits an electric field to induce its cofactor PLP and substrates into the active site. Based on the molecular docking simulations, we concluded that the orientations of the functional groups and amino group at the chiral center of an amino group donor comprise determining factors for the (*S*)-enantioselectivity of Tr- ω TA. In addition, pyruvate as an amino group acceptor was assumed to bind to the R416 residue, attaining binding stability at the active site. To more specifically understand the catalytic mechanism of Tr- ω TA, it is necessary to elucidate the stepwise intermediate states on the basis of structural information. Thus, future work should determine the respective complex structures by crystallizing the substrate-bound forms of Tr- ω TA. Nevertheless, our results lay the groundwork for a more comprehensive understanding of the transamination mechanism.

Methods

Cloning, overexpression, and purification. The pET24a(+) expression vector for Tr- ω TA was constructed. The plasmid was delivered into *Escherichia coli* BL21(DE3) for transformation. A single colony was selected and cultured in lysogeny broth medium containing 50 μ g/ml kanamycin at 37 $^{\circ}$ C overnight. The resulting cells were cultured on a large scale at 37 $^{\circ}$ C until the optical density value at 600 nm reached approximately 0.6. Overexpression of the gene was induced with 0.5 mM isopropyl β -D-1-thiogalactopyranoside and the cells

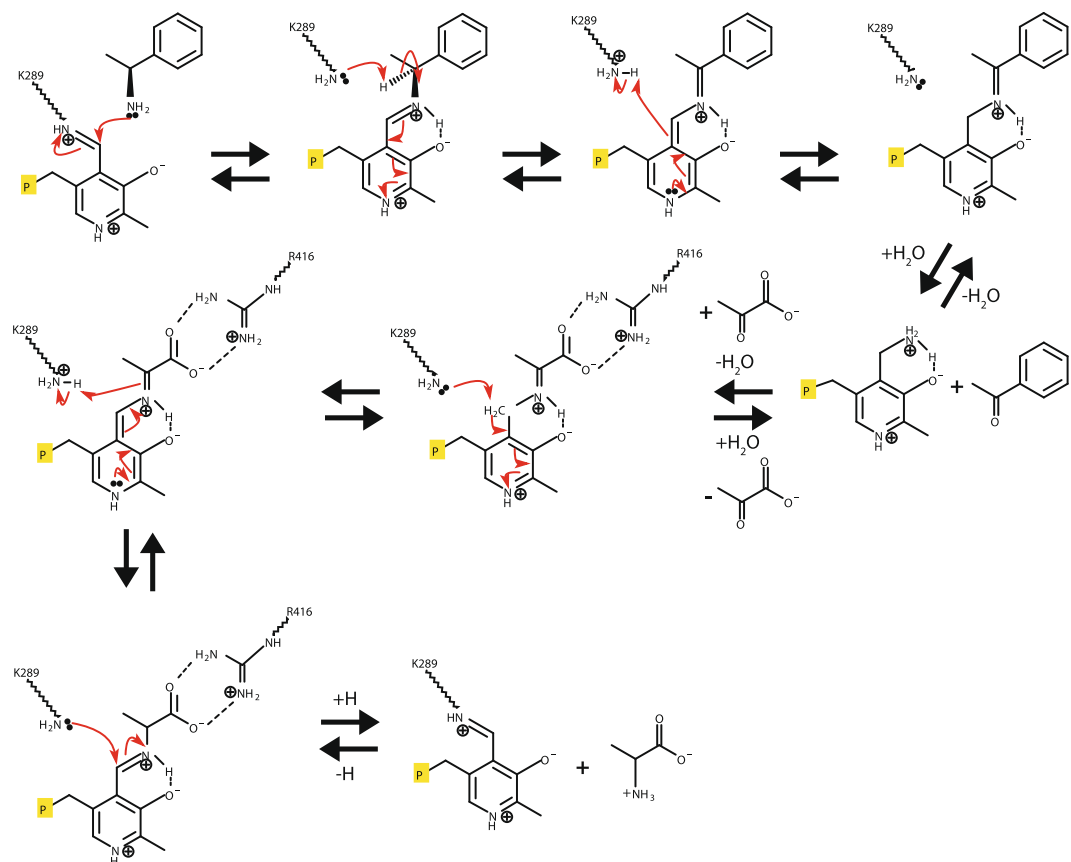


Figure 8. Proposed catalysis mechanism for Tr- ω TA. (*S*)- α -MBA and pyruvate are used as model substrates for amino group donation and acceptance, respectively. The red arrows denote the attack directions of a pair of electrons. The yellow-boxed P letter symbolizes the phosphate group of the PLP/PMP cofactor.

were further cultured at 20 °C for 18 h. The cultured cells were harvested by centrifugation, washed with buffer A [20 mM Tris-HCl (pH 8.0), 500 mM NaCl, and 20 mM imidazole], flash-frozen with liquid N₂, and stored at -80 °C until use.

The cell pellet was resuspended with buffer A supplemented with phenylmethanesulfonyl fluoride (Sigma-Aldrich) as a serine protease inhibitor and lysed by sonication on ice using 30-s bursts with a 1-min time interval between each burst. The cell debris was removed by centrifugation at 10,000 g for 30 min at 4 °C. The supernatant was mixed with Ni-nitrilotriacetic acid resins by gentle agitation overnight. The mixture was loaded onto a gravity-flow column pre-equilibrated with buffer A. The column was washed with buffer B [20 mM Tris-HCl (pH 8.0), 500 mM NaCl, and 60 mM imidazole] twice. Then, the Tr- ω TA protein was eluted with buffer C [20 mM Tris-HCl (pH 8.0), 500 mM NaCl, and 250 mM imidazole]. The eluate was loaded onto a Superdex 200 Increase 10/300 GL 24 ml column (GE Healthcare) pre-equilibrated with buffer D [20 mM Tris-HCl (pH 8.0), 150 mM NaCl]. SEC purification was performed using an ÄKTA explorer system (GE Healthcare). Protein fractions were harvested, concentrated to 10 mg/ml using a centrifugal 0.2- μ m filter, flash-frozen in liquid N₂, and stored at -80 °C until use for crystallization experiments. All of the purification fractions were analyzed by SDS-PAGE.

Crystallization and data collection. The initial crystallization conditions were screened using commercial screening kits such as Wizard I and II (Hampton Research). Crystals were initially obtained from a buffer condition consisting of 1 M sodium citrate tribasic and 0.1 M imidazole/HCl (pH 8.0). The crystallization condition was optimized by modulating buffer concentration and pH, and supplementing an additive. For droplet preparation, 1 μ l of protein solution was mixed with an equal volume of reservoir solution. Each droplet was equilibrated against 400 μ l of the mother liquor using the hanging drop vapor diffusion method at 20 °C. Diffraction-quality crystals appeared in 10 days under a buffer condition of 0.9 M sodium citrate tribasic, 0.1 M imidazole/HCl (pH 7.4), and 0.1 M betaine-HCl. The crystals were soaked in a cryoprotectant solution comprising the reservoir solution supplemented with 15% (v/v) glycerol. Then, the crystals were mounted onto a goniometer head and flash-cooled in a N₂ stream at -178 °C. X-ray diffraction data for Tr- ω TA were collected at the PAL 5C beamline (Pohang, Korea). Indexing, integrating, and scaling of the diffraction data were processed using HKL2000 software³⁵.

Structure determination and refinement. The phase of Tr- ω TA was determined by molecular replacement using Phaser-MR³⁶ in Phenix³⁷. The structure of Vf- ω TA (PDB ID: 4E3Q) was used as a search model. The

initial model of Tr- ω TA was automatically built with AutoBuild³⁸ in Phenix, and a portion was manually built using Coot³⁹. Iterative cycles of refinement were run using phenix.refine⁴⁰ in Phenix. The model refinement was finished when R_{work} and R_{free} values reached 15.3% and 15.5%, respectively. Validation for the final model was performed using MolProbity⁴¹.

Multiple sequence alignment was performed and displayed using Clustal Omega⁴² and ESPript 3.0 (<http://esprict.ibcp.fr>)⁴³, respectively. All the structural figures shown in this study were prepared using Pymol⁴⁴.

Molecular docking simulations. Substrate candidates for Tr- ω TA were prepared using Avogadro⁴⁵. All the structures were energetically minimized. Molecular docking simulations were performed using Autodock Vina⁴⁶, a program package for molecular docking. AutoDockTools 1.5.6⁴⁷ was used to generate the pdbqt files of Tr- ω TA and the compounds. The active site-forming residues such as L23, W61, Y154, I263, K289 from subunit B, and F89 from subunit A were designated as flexible residues and the rest residues were set to rigid residues during the docking simulations. The size and spacing of a grid box including the flexible residues were set to 20 Å × 20 Å × 20 Å and 1 Å, respectively. Other parameters were assigned default values. A total of 15 different conformers per docking compound were generated. The docking results were ranked using an energy scoring function.

Multiangle light scattering analysis. A SEC-MALS analysis was conducted to measure the absolute molecular weight of Tr- ω TA in solution. The protein solution was loaded onto a Superdex 200 10/300 GL 24 ml column pre-equilibrated with a buffer comprising 20 mM Tris-HCl (pH 8.0) and 500 mM NaCl. The mobile phase was pumped at a flow rate of 0.4 ml/min at room temperature. A DAWN-treos MALS detector (Wyatt Technology) was used in conjunction with an ÅKTA explorer system. BSA was used as a reference. Data were assessed using ASTRA software provided by Wyatt Technology.

UV-Visible spectroscopic analysis. A UV-Visible absorption spectroscopic analysis for Tr- ω TA was carried out using NanoPhotometer NP80 spectrophotometry (IMPEL) to specify a cofactor in Tr- ω TA. The light was generated using a xenon flash lamp with a bandwidth of 1.8 nm. An absorption spectrum was obtained from a wavelength range of 200–900 nm. Wavelengths for peak absorbance were analyzed to identify corresponding molecules.

Data Availability

The atomic coordinates and structure factors for Tr- ω TA have been deposited in the Protein Data Bank (<http://www.rcbs.org>) under accession number 6IO1.

References

- Malik, M. S., Park, E. S. & Shin, J. S. Features and technical applications of ω -transaminases. *Appl Microbiol Biotechnol.* **94**, 1163–1171 (2012).
- Bezsudnova, E. Y., Boyko, K. M. & Popov, V. O. Properties of bacterial and archaeal branched-chain amino acid aminotransferases. *Biochemistry (Moscow)* **82**, 1572–1591 (2017).
- Fuchs, M., Farnberger, J. E. & Kroutil, W. The industrial age of biocatalytic transamination. *Eur J Org Chem.* **32**, 6965–6982 (2015).
- Guo, F. & Berglund, P. Transaminase biocatalysis: optimization and application. *Green Chem.* **19**, 333–360 (2017).
- Slabu, I., Galman, J. L., Lloyd, R. C. & Turner, N. J. Discovery, engineering, and synthetic application of transaminase biocatalysts. *ACS Catal.* **7**, 8263–8284.
- Toney, M. D. Controlling reaction specificity in pyridoxal phosphate enzymes. *Biochim Biophys Acta* **1814**, 1407–1418 (2017).
- Park, E. S., Kim, M. & Shin, J. S. Molecular determinants for substrate selectivity of ω -transaminases. *Appl Microbiol Biotechnol.* **93**, 2425–2435 (2012).
- Schirolli, D. & Peracchi, A. A subfamily of PLP-dependent enzymes specialized in handling terminal amines. *Biochim Biophys Acta* **1854**, 1200–1211 (2015).
- Soda, K., Yoshimura, T. & Esaki, N. Stereospecificity for the hydrogen transfer of pyridoxal enzyme reactions. *Chem Rec.* **1**, 373–384 (2001).
- Oosterwijk, N. V. *et al.* Structural basis of the substrate range and enantioselectivity of two (S)-selective ω -transaminases. *Biochemistry* **55**, 4422–4431 (2016).
- Nakamichi, K., Shibatani, T., Yamamoto, Y. & Sato, T. Asymmetric amination of 4-methoxyphenylacetone and its related compounds with microorganisms. *Appl Microbiol Biotechnol.* **33**, 637–640 (1990).
- Shin, J. S. & Kim, B. G. Comparison of the ω -transaminases from different microorganisms and application to production of chiral amines. *Biosci Biotech Biochem.* **65**, 1782–1788 (2001).
- Shin, J. S. & Kim, B. G. Exploring the active site of amine:pyruvate aminotransferase on the basis of the substrate structure-reactivity relationship: how the enzyme controls substrate specificity and stereoselectivity. *J Org Chem.* **67**, 2848–2853 (2002).
- Kaulmann, U., Smithies, K., Smith, K. E. B., Hailes, H. C. & Ward, J. M. Substrate spectrum of ω -transaminase from *Chromobacterium violaceum* DSM30191 and its potential for biocatalysis. *Enzyme Microb Technol.* **41**, 628–637 (2007).
- Hanson, R. L. *et al.* Preparation of (R)-amines from racemic amines with an (S)-amine transaminase from *Bacillus megaterium*. *Adv Synth Catal.* **350**, 1367–1375 (2008).
- Hwang, B. Y. *et al.* Identification of ω -aminotransferase from *Caulobacter crescentus* and site-directed mutagenesis to broaden substrate specificity. *J Microbiol Biotechnol.* **18**, 48–54 (2008).
- Koszelewski, D., Göritzer, M., Clay, D., Seisser, B. & Kroutil, W. Synthesis of optically active amines employing recombinant ω -transaminases in *E. coli* cells. *ChemCatChem* **2**, 73–77 (2010).
- Koszelewski, D., Tauber, K., Faber, K. & Kroutil, W. ω -transaminases for the synthesis of non-racemic α -chiral primary amines. *Trends Biotechnol.* **28**, 324–332 (2010).
- Park, E., Kim, M. & Shin, J. S. One-pot conversion of L-threonine into L-homoalanine: biocatalytic production of an unnatural amino acid from a natural one. *Adv Synth Catal.* **352**, 3391–3398 (2010).
- Watanabe, N. *et al.* Crystal structure analysis of omega-amino acid:pyruvate aminotransferase with a newly developed Weissenberg camera and an imaging plate using synchrotron radiation. *J Biochem.* **105**, 1–3 (1989).
- Humble, M. S. *et al.* Crystal structures of the *Chromobacterium violaceum* ω -transaminase reveal major structural rearrangement upon binding of coenzyme PLP. *FEBS J.* **279**, 779–792 (2012).

22. Sayer, C., Isupov, M. N., Westlake, A. & Littlechild, J. A. Structural study of *Pseudomonas* and *Chromobacterium* ω -aminotransferases provide insights into their differing substrate specificity. *Acta Crystallogr D Biol Crystallogr.* **69**, 564–576 (2013).
23. Guan, L. J. *et al.* A new target region for changing the substrate specificity of amine transaminases. *Sci Rep.* **5**, 10753 (2015).
24. Deepankumar, K. *et al.* Enhancing thermostability and organic solvent tolerance of ω -transaminase through global incorporation of fluorotyrosine. *Adv Synth Catal.* **356**, 993–998 (2014).
25. Shin, Y. C., Yun, H. & Park, H. H. Structural dynamics of the transaminase active site revealed by the crystal structure of a co-factor free omega-transaminase from *Vibrio fluvialis* JS17. *Sci Rep.* **8**, 11454 (2018).
26. Midelfort, K. S. *et al.* Redesigning and characterizing the substrate specificity and activity of *Vibrio fluvialis* aminotransferase for the synthesis of imagabalin. *Protein Eng Des Sel.* **26**, 25–33 (2013).
27. Mathew, S. *et al.* Identification of novel thermostable ω -transaminase and its application for enzymatic synthesis of chiral amines at high temperature. *RSC Adv.* **6**, 69257–69260 (2016).
28. Krissinel, E. & Henrick, K. Inference of macromolecular assemblies from crystalline state. *J Mol Biol.* **372**, 774–797 (2007).
29. Boyko, K. M. *et al.* First structure of archaeal branched-chain amino acid aminotransferase from *Thermoproteus uzoniensis* specific for L-amino acids and R-amines. *Extremophiles* **20**, 215–225 (2016).
30. Vihiner, M. Relationship of protein flexibility to thermostability. *Protein Eng.* **1**, 477–480 (1987).
31. Malashkevich, V. N., Onuffer, J. J., Kirsch, J. F. & Jansonius, J. N. Alternating arginine-modulated substrate specificity in an engineering tyrosine aminotransferase. *Nat Struct Biol.* **2**, 548–553 (1995).
32. Toney, M. D. & Kirsch, J. F. Brønsted analysis of aspartate aminotransferase via exogenous catalysis of reactions of an inactive mutant. *Protein Sci.* **1**, 107–119 (1992).
33. Ripoll, D. R., Faerman, C. H., Axelsen, P. H., Silman, I. & Sussman, J. L. An electrostatic mechanism for substrate guidance down the aromatic gorge of acetylcholinesterase. *Proc Natl Acad Sci USA* **90**, 5128–5132 (1993).
34. Wade, R. C., Gabdouliline, R. R., Ludemann, S. K. & Lounnas, V. Electrostatic steering and ionic tethering in enzyme-ligand binding: Insights from simulations. *Proc Natl Acad Sci USA* **95**, 5942–5949 (1998).
35. Otwinowski, Z. & Minor, W. Processing of X-ray Diffraction Data Collected in Oscillation Mode. *Methods Enzymol.* **276**, 307–326 (1997).
36. McCoy, A. J. *et al.* Phaser crystallographic software. *J Appl Crystallogr.* **40**, 658–674 (2007).
37. Adams, P. D. *et al.* PHENIX: a comprehensive Python-based system for macromolecular structure solution. *Acta Crystallogr D Biol Crystallogr.* **66**, 213–221 (2010).
38. Terwilliger, T. C. *et al.* Iterative model building, structure refinement and density modification with the PHENIX AutoBuild wizard. *Acta Crystallogr D Biol Crystallogr.* **64**, 61–69 (2008).
39. Emsley, P. & Cowtan, K. Coot: model-building tools for molecular graphics. *Acta Crystallogr D Biol Crystallogr.* **60**, 2126–2132 (2004).
40. Afonine, P. V. *et al.* Towards automated crystallographic structure refinement with phenix.refine. *Acta Crystallogr D Biol Crystallogr.* **68**, 352–367 (2012).
41. Chen, V. B. *et al.* MolProbity: all-atom structure validation for macromolecular crystallography. *Acta Crystallogr D Biol Crystallogr.* **66**, 12–21 (2010).
42. Sievers, F. *et al.* Fast, scalable generation of high-quality protein multiple sequence alignments using Clustal Omega. *Mol Syst Biol.* **7**, 1–6 (2007).
43. Robert, X. & Gouet, P. Deciphering key features in protein structures with the new ENDscript server. *Nucl Acids Res.* **42**, 320–324 (2014).
44. The PyMOL Molecular Graphics System, Version 1.7.4 Schrödinger, LLC. Available online, <http://www.pymol.org> (2015).
45. Hanwell, M. D. *et al.* Avogadro: An advanced semantic chemical editor, visualization, and analysis platform. *J Cheminform* **4**, 1–17 (2012).
46. Trott, O. & Olson, A. J. Auto DockVina: improving the speed and accuracy of docking with a new scoring function, efficient optimization and multithreading. *J Comput Chem.* **31**, 455–461 (2010).
47. Morris, G. M. *et al.* Autodock4 and AutoDockTools4: automated docking with selective receptor flexibility. *J Comput Chem.* **16**, 2785–2791 (2009).

Acknowledgements

This work was supported by National Research Foundation of Korea (NRF) grant funded by the Korea government (NRF-2017M3A9D8062960 and NRF-2018R1A4A1023822), and a grant from Korea Polar Research Institute (Grant Number PE19210).

Author Contributions

H.H.P. designed and supervised the project. S.K. performed all experiments from cloning to determination of the structure along with molecular docking simulations and data analysis. C.M.K. H.J. and J.H.L. performed MALS. J.H.J., H.Y. and I.S. performed UV-Visible spectroscopy. H.H.P. and S.K. wrote the manuscript. All authors discussed the results, commented on the manuscript, and approved the manuscript.

Additional Information

Supplementary information accompanies this paper at <https://doi.org/10.1038/s41598-019-43490-2>.

Competing Interests: The authors declare no competing interests.

Publisher's note: Springer Nature remains neutral with regard to jurisdictional claims in published maps and institutional affiliations.



Open Access This article is licensed under a Creative Commons Attribution 4.0 International License, which permits use, sharing, adaptation, distribution and reproduction in any medium or format, as long as you give appropriate credit to the original author(s) and the source, provide a link to the Creative Commons license, and indicate if changes were made. The images or other third party material in this article are included in the article's Creative Commons license, unless indicated otherwise in a credit line to the material. If material is not included in the article's Creative Commons license and your intended use is not permitted by statutory regulation or exceeds the permitted use, you will need to obtain permission directly from the copyright holder. To view a copy of this license, visit <http://creativecommons.org/licenses/by/4.0/>.

© The Author(s) 2019